Monthly Notices
of the
ROYAL ASTRONOMICAL SOCIETY

Mon. Not. R. Astron. Soc. **426,** 1613–1631 (2012) doi:10.1111/j.1365-2966.2012.21821.x

General relativistic radiation hydrodynamics of accretion flows – II. Treating stiff source terms and exploring physical limitations

C. Roedig,[1⋆] O. Zanotti[2] and D. Alic[1]

[1]*Max-Planck-Institut für Gravitationsphysik, Albert Einstein Institut, Am Mühlenberg 1, D-14476 Golm, Germany*
[2]*Università di Trento, Laboratorio di Matematica Applicata, Via Messiano 77, I-38100 Trento, Italy*

Accepted 2012 July 28. Received 2012 July 28; in original form 2012 June 28

ABSTRACT

We present the implementation of an implicit–explicit (IMEX) Runge–Kutta numerical scheme for general relativistic (GR) hydrodynamics coupled to an optically thick radiation field in two existing GR-(magneto)hydrodynamics codes. We argue that the necessity of such an improvement arises naturally in most astrophysically relevant regimes where the optical thickness is high as the equations become stiff. By performing several simple 1D tests, we verify the codes' new ability to deal with this stiffness and show consistency. Then, still in one spatial dimension, we compute a luminosity versus accretion rate diagram for the set-up of spherical accretion on to a Schwarzschild black hole and find good agreement with previous work which included more radiation processes than we currently have available. Lastly, we revisit the supersonic Bondi–Hoyle–Lyttleton (BHL) accretion in two dimensions where we can now present simulations of realistic temperatures, down to $T \sim 10^6$ K or less. Here we find that radiation pressure plays an important role, but also that these highly dynamical set-ups push our approximate treatment towards the limit of physical applicability. The main features of radiation hydrodynamics BHL flows manifest as (i) an effective adiabatic index approaching $\gamma_{\rm eff} \sim 4/3$; (ii) accretion rates two orders of magnitude lower than without radiation pressure, but still super-Eddington; (iii) luminosity estimates around the Eddington limit, hence with an overall radiative efficiency as small as $\eta_{\mathcal{BHL}} \sim 10^{-2}$; (iv) strong departures from thermal equilibrium in shocked regions; (v) no appearance of the flip-flop instability. We conclude that the current optically thick approximation to the radiation transfer does give physically substantial improvements over the pure hydro also in set-ups departing from equilibrium, and, once accompanied by an optically thin treatment, is likely to provide a fundamental tool for investigating accretion flows in a large variety of astrophysical systems.

Key words: accretion, accretion discs – black hole physics – radiative transfer – methods: numerical.

1 INTRODUCTION

The field of numerical relativistic hydrodynamics has recently seen much progress in treating astrophysical systems under more and more realistic conditions. Because of the large computational costs involved, the inclusion of multidimensional general relativistic radiation hydrodynamics (GR-RHD) has been postponed for a long time, with the remarkable exception of neutrino transport in the context of supernova simulations (see Lentz et al. 2012 and references therein). However, due to the increasing power of supercomputers, the situation has started changing significantly in the last few years, and the inclusion of a photon field is no longer regarded as a remote possibility.

This delay has, however, not been due to the fact that dynamical radiation fields are not regarded as a main ingredient, rather it is the inherent difficulty of solving the radiation transfer equation.[1] The cooling time-scales of a dynamical fluid may easily vary over several orders of magnitude within the computational domain. This then leads to characteristic propagation speeds for the photons in optically thin regions that are much higher than the coupled fluid/photon speeds in optically thick regions. Not only are time-scales vastly different, but also additional spatial resolution is required whenever the coupling to the photon field induces small-scale instabilities and turbulence. In addition,

⋆E-mail: croedig@aei.mpg.de

[1] See Pomraning (1973) and Mihalas & Mihalas (1984) for a comprehensive treatment of RHD and Schweizer (1988) for the extension to the relativistic case.

surfaces of astrophysical structures are typically not in local thermal equilibrium (LTE) and can cool very efficiently, usually on much shorter time-scales than the dynamical ones. This problem becomes particularly severe when performing global simulations of astrophysical systems in which the principal force is gravity. In these cases, first the spatial domain must be large enough to contain the entire astrophysical structure and secondly, it needs to resolve the influence of gravity.[2]

Any such multiscale problem is numerically extremely costly and it is thus important to formulate efficient algorithms that include at least a leading order approximation to the various physics while still remaining computationally affordable. One of the most successful strategies was, and still is, represented by the so-called projected symmetric trace-free (PSTF) moment formalism introduced by Thorne (1981). By defining moments of the radiation field similarly to how density, momentum and pressure of a fluid are defined as velocity moments of the corresponding distribution function, such a formalism provides an accurate, though still reasonably cheap, approximation to the solution of the radiation transfer equations. This approach is particularly appealing in the case of an optically thick medium, characterized by a strong coupling between matter and radiation. Farris et al. (2008) were first to undertake the implementation of the corresponding RHD equations in a GR framework. A further step has been taken by Shibata et al. (2011), who adopted the variable Eddington factor approach of Levermore (1984) to solve the relativistic RHD equations both in the optically thin and in the optically thick limit. This represents a significant progress with respect to simplified treatments, where effective cooling functions are introduced.

In spite of all this progress, major numerical difficulties still prevent the application of such schemes to realistic astrophysical systems; one of them being the presence of stiff source terms. For example, in Zanotti et al. (2011, hereafter Paper I), after implementing and testing the framework suggested by Farris et al. (2008), we studied the Bondi–Hoyle–Lyttleton (BHL) accretion flow on to a black hole, but we could only treat unrealistically high fluid temperatures of the order of $\sim 10^9$ K or above. Though simplified, the BHL flow can effectively help our understanding of those compact sources accreting matter with a reduced amount of angular momentum, and is currently applied to the study of both high-mass X-ray binaries (Hadrava & Čechura 2012) and of the merging of supermassive black hole binaries (see Pfeiffer 2012 and references therein).

In this paper, we address the problem of treating the optically thick regime compatible with the conservative formulation used in Eulerian GR magnetohydrodynamic (MHD) codes, while at the same time coping with the stiffness of the source terms. As a stiff solver, we choose the implicit–explicit (IMEX) scheme by Pareschi & Russo (2005), implement it in both WHISKY[3] and ECHO,[4] and test the codes against each other. As the two codes contain internal differences, such as scheduling and general infrastructure, it is very useful to validate both of them at this stage, even though the main part of the simulations shown in this paper is performed with ECHO because of its spherical, non-uniform grid.[5]

This paper is organized as follows. In Section 2, we describe the treatment of the radiation stiff source terms. We detail an IMEX Runge–Kutta (RK) scheme as our time integration stiff solver. Section 3 presents the verification of our new scheme through a selected sample of stiff shock-tube problems. Turning towards astrophysical applications, we first present in Section 4 the results for spherical accretion in a regime that was constructed to be particularly challenging for the numerics. We also present a physical Michel solution and compare it with previous results. Abandoning spherical symmetry, we devote Section 5 to the study of the RHD of BHL accretion in two dimensions. Finally, in Section 6 we offer a brief summary and our conclusions.

Throughout the paper, we set the speed of light $c = 1$, and the gravitational constant G to a pure number. We extend the geometric units by setting $m_{\rm p}/k_{\rm B} = 1$, where $m_{\rm p}$ is the mass of the proton and $k_{\rm B}$ is the Boltzmann constant. However, we have maintained c, G and $k_{\rm B}$ in an explicit form in those expressions of particular physical interest. We refer the interested reader to appendix A of Paper I for the system of extended geometrized units.

2 RADIATION HYDRODYNAMICS IN THE STIFF REGIME

2.1 Formulation of the GR-RHD equations

In this section, we first review the set of equations that we use to approximate GR-RHD in the diffusion limit, as derived in Farris et al. (2008) and already implemented and verified in Paper I. The properties of the fluid immersed in the radiation field are described by the momentum-energy tensor, which is given by

$$\boldsymbol{T}^{\alpha\beta} = \boldsymbol{T}^{\alpha\beta}_{\rm m} + \boldsymbol{T}^{\alpha\beta}_{\rm r}, \tag{1}$$

and comprises a matter contribution

$$\boldsymbol{T}^{\alpha\beta}_{\rm m} = \rho h\, u^{\alpha} u^{\beta} + P g^{\alpha\beta} \tag{2}$$

and a radiation contribution

$$\boldsymbol{T}^{\alpha\beta}_{\rm r} = \frac{1}{c} \int I_{\nu} N^{\alpha} N^{\beta} \mathrm{d}\nu\, \mathrm{d}\Omega, \tag{3}$$

[2] A complementary approach, which is not covered here, is to model not a global system, but only a small, representative region, e.g. a shearing box.
[3] www.whiskycode.org
[4] Del Zanna et al. (2007).
[5] WHISKY uses Cartesian adaptive mesh refinement, which is less suited for spherical models.

where $g^{\alpha\beta}$ is the metric of the space–time, u^α is the four-velocity of the fluid, ρ, $h = 1 + \epsilon + P/\rho$, ϵ and P are the rest-mass density, the specific enthalpy, the specific internal energy and the thermal pressure, respectively, while $I_\nu = I_\nu(x^\alpha, N^i, \nu)$ is the specific intensity of the radiation. We note that N^α defines the propagation direction of the photon with frequency ν, while $\mathrm{d}\Omega$ is the infinitesimal solid angle around N^α. All of these quantities are measured in the comoving frame of the fluid. The thermal pressure is related to ρ and ϵ through an equation of state (EoS), which we take to be that of the ideal gas, with constant adiabatic index γ, i.e.

$$P = \rho\epsilon(\gamma - 1)\,. \tag{4}$$

In terms of the moments of the radiation field (Thorne 1981), the radiation energy-momentum tensor $\boldsymbol{T}_{\rm r}^{\alpha\beta}$ can be rewritten as (Hsieh & Spiegel 1976)

$$\boldsymbol{T}_{\rm r}^{\alpha\beta} = (E_{\rm r} + \mathcal{P}_{\rm r})u^\alpha u^\beta + F_{\rm r}^\alpha u^\beta + u^\alpha F_{\rm r}^\beta + \mathcal{P}_{\rm r} g^{\alpha\beta}, \tag{5}$$

where $E_{\rm r}$ and $\mathcal{P}_{\rm r}$ are the radiation energy density and pressure, respectively. We make the additional assumption that the radiation field is approximately isotropic, in the sense that $\mathcal{P}_{\rm r} = E_{\rm r}/3$, while the radiation flux is not constrained to zero, but is allowed to take small values such that $F_{\rm r}^i/E_{\rm r} \ll 1$. Thus, the equations governing the evolution of the system are

$$\nabla_\alpha(\rho u^\alpha) = 0, \tag{6}$$

$$\nabla_\alpha \boldsymbol{T}^{\alpha\beta} = 0, \tag{7}$$

$$\nabla_\alpha \boldsymbol{T}_{\rm r}^{\alpha\beta} = -G_{\rm r}^\beta, \tag{8}$$

where $G_{\rm r}^\alpha = G_{\rm r}^\alpha(I, \chi^{\rm t}, \chi^{\rm s})$, called the radiation four-force density, depends on the specific intensity and on the opacities of the matter interaction. As in Paper I, we drop all frequency dependencies and allow for small deviations from LTE. We consider bremsstrahlung and Thomson scattering (i.e. $\chi^{\rm t}$ and $\chi^{\rm s}$) as processes of absorption and scattering. Using the Planck function, $\tilde{B}$, it is then possible to write the radiation four-force in covariant form as (Farris et al. 2008)

$$G_{\rm r}^\alpha = \chi^{\rm t}(E_{\rm r} - 4\pi\tilde{B})u^\alpha + (\chi^{\rm t} + \chi^{\rm s})F_{\rm r}^\alpha\,. \tag{9}$$

In equation (9) we have introduced the equilibrium blackbody intensity $4\pi\tilde{B} = a_{\rm rad}T_{\rm fluid}^4$, where $T_{\rm fluid}$ is the temperature of the fluid and $a_{\rm rad}$ is the radiation constant. We estimate the temperature from the ideal-gas EoS via the expression

$$T_{\rm fluid} = \frac{m_{\rm p}}{k_{\rm B}}\frac{P}{\rho}, \tag{10}$$

where $k_{\rm B}$ is the Boltzmann constant and $m_{\rm p}$ is the rest mass of the proton. We stress that the method allows for deviations from thermal equilibrium, namely with $E_{\rm r} \neq 4\pi\tilde{B}$. As shown in Paper I, after adopting the $3 + 1$ split of space–time (Arnowitt, Deser & Misner 1962) the GR-RHD equations can be written in conservative form as

$$\partial_t \boldsymbol{\mathcal{U}} + \partial_i \boldsymbol{\mathcal{F}}^i = \boldsymbol{\mathcal{S}}, \tag{11}$$

where the vector of conserved variables $\boldsymbol{\mathcal{U}}$ and the fluxes $\boldsymbol{\mathcal{F}}^i$ are given by

$$\boldsymbol{\mathcal{U}} \equiv \sqrt{\mathfrak{s}}\begin{bmatrix} D \\ S_j \\ U \\ U_{\rm r} \\ (S_{\rm r})_j \end{bmatrix}, \quad \boldsymbol{\mathcal{F}}^i \equiv \sqrt{\mathfrak{s}}\begin{bmatrix} \alpha v^i D - \beta^i D \\ \alpha W^i{}_j - \beta^i S_j \\ \alpha S^i - \beta^i U \\ \alpha S_{\rm r}^i - \beta^i U_{\rm r} \\ \alpha(R_{\rm r})^i_j - \beta^i (S_{\rm r})_j \end{bmatrix}, \tag{12}$$

while the sources are

$$\boldsymbol{\mathcal{S}} \equiv \sqrt{\mathfrak{s}}\begin{bmatrix} 0 \\ \frac{1}{2}\alpha W^{ik}\partial_j \mathfrak{s}_{ik} + S_i\partial_j\beta^i - U\partial_j\alpha + \alpha(G_{\rm r})_j \\ \frac{1}{2}W^{ik}\beta^j\partial_j\mathfrak{s}_{ik} + W_i{}^j\partial_j\beta^i - S^j\partial_j\alpha + \alpha^2 G_{\rm r}^t \\ \frac{1}{2}R_{\rm r}^{ik}\beta^j\partial_j\mathfrak{s}_{ik} + (R_{\rm r})_i^j\partial_j\beta^i - S_{\rm r}^j\partial_j\alpha - \alpha^2 G_{\rm r}^t \\ \frac{1}{2}\alpha R_{\rm r}^{ik}\partial_j\mathfrak{s}_{ik} + (S_{\rm r})_i\partial_j\beta^i - U_{\rm r}\partial_j\alpha - \alpha(G_{\rm r})_j \end{bmatrix}. \tag{13}$$

We note that α, β and $\mathfrak{s}$ are the lapse, the shift and the determinant of the spatial metric, while v^i and Γ are the three-velocity and the Lorentz factor of the fluid with respect to the Eulerian observer, respectively. In equations (12) and (13) several more terms have been defined, which we report below for completeness (cf. Paper I for more details):

$$W^{ij} \equiv \rho h\Gamma^2 v^i v^j + P\,\mathfrak{s}^{ij}, \tag{14}$$

$$S^i \equiv \rho h\Gamma^2 v^i, \tag{15}$$

$$U \equiv \rho h\Gamma^2 - P, \tag{16}$$

$$R^{ij}_{\rm r} = \frac{4}{3}E_{\rm r}\Gamma^2 v^i v^j + \Gamma\left(f^i_{\rm r} v^j + f^j_{\rm r} v^i\right) + \mathcal{P}_{\rm r}\mathfrak{s}^{ij}, \tag{17}$$

$$S^i_{\rm r} = \frac{4}{3}E_{\rm r}\Gamma^2 v^i + \Gamma\left(\alpha F^t_{\rm r} v^i + f^i_{\rm r}\right), \tag{18}$$

$$U_{\rm r} = \frac{4}{3}E_{\rm r}\Gamma^2 + 2\alpha\Gamma F^t_{\rm r} - \frac{E_{\rm r}}{3}, \tag{19}$$

$$F^t_{\rm r} = \frac{v_i F^i_{\rm r}}{\alpha - \beta_i v^i} = \frac{v_i f^i_{\rm r}}{\alpha}\,. \tag{20}$$

2.2 Description of the IMEX scheme for radiation hydrodynamics

2.2.1 General concepts

A relevant feature of the RHD equations (11) is that they contain sources for the radiation field that may easily become stiff, depending on the physical conditions under consideration. When stiffness is treated by resorting to IMEX RK schemes,[6] it is important to split the conservative variables $\boldsymbol{\mathcal{U}}$ in two subsets $\{\boldsymbol{X}, \boldsymbol{Y}\}$, with $\{\boldsymbol{X}\}$ containing the variables that are affected by stiffness and $\{\boldsymbol{Y}\}$ containing those that are not. IMEX RK methods are based on an implicit discretization for the stiff terms and on an explicit one for the non-stiff terms. They have been extensively discussed in a series of papers by Pareschi & Russo (2005), and some recent applications have been presented in special relativistic resistive MHD by Palenzuela et al. (2009), in GR force-free electrodynamics by Alic et al. (2012) and in GR resistive MHD by Bucciantini & Del Zanna (2012) and Dionysopoulou et al. (2012). In full generality, the hyperbolic equations for the two sets of variables $\{\boldsymbol{X}, \boldsymbol{Y}\}$ are split as

$$\partial_t \boldsymbol{Y} = \boldsymbol{F}_Y(\boldsymbol{X}, \boldsymbol{Y}), \tag{21}$$

$$\partial_t \boldsymbol{X} = \boldsymbol{F}_X(\boldsymbol{X}, \boldsymbol{Y}) + \boldsymbol{R}_X(\boldsymbol{X}, \boldsymbol{Y}), \tag{22}$$

where the operator $\boldsymbol{F}_Y$ contains both the first spatial derivatives of $\boldsymbol{Y}$ and non-stiff source terms, the operator $\boldsymbol{F}_X$ contains both the first spatial derivatives of $\boldsymbol{X}$ and non-stiff source terms, while the operator $\boldsymbol{R}_X$ contains the stiff source terms affecting the variables $\boldsymbol{X}$. Each RK substage of the IMEX scheme can be divided in two parts.

(i) In the first part, the explicit intermediate values $\{\boldsymbol{X}^{*,i}, \boldsymbol{Y}^{*,i}\}$ of each substage i are computed as

$$\boldsymbol{Y}^{*,i} = \boldsymbol{Y}^n + \Delta t \sum_{j=1}^{i-1} \tilde{a}_{ij} \boldsymbol{F}_Y[\boldsymbol{\mathcal{U}}^{(j)}], \tag{23}$$

$$\boldsymbol{X}^{*,i} = \boldsymbol{X}^n + \Delta t \sum_{j=1}^{i-1} \tilde{a}_{ij} \boldsymbol{F}_X[\boldsymbol{\mathcal{U}}^{(j)}] + \Delta t \sum_{j=1}^{i-1} a_{ij} \boldsymbol{R}_X[\boldsymbol{\mathcal{U}}^{(j)}], \tag{24}$$

where one might note that the summation stops at $(i-1)$, in order to avoid the appearance of the implicit terms at this stage. The matrices $(\tilde{a}_{ij})$ and (a_{ij}) are $\nu \times \nu$ square matrices. In this paper, we use $\nu = 4$ (see also Appendix B), whereas, in general, the matrix coefficients and dimensions change with the desired number of stages[7] (Pareschi & Russo 2005).

(ii) In the second part, the non-stiff variables are directly advanced to the status of substage RK variables, namely

$$\boldsymbol{Y}^{(i)} = \boldsymbol{Y}^{*,i}, \tag{25}$$

while the stiff variables need to be corrected as

$$\boldsymbol{X}^{(i)} = \mathbf{M}(\boldsymbol{Y}^{*,i})\left[\boldsymbol{X}^{*,i} + a_{ii}\Delta t \boldsymbol{K}_X(\boldsymbol{Y}^{*,i})\right]\,. \tag{26}$$

The vector $\boldsymbol{K}_X(\boldsymbol{Y})$ on the right-hand side of equation (26), which does not depend on the stiff variables $\boldsymbol{X}$, results from the decomposition of $\boldsymbol{R}_X(\boldsymbol{X}, \boldsymbol{Y})$ as

$$\boldsymbol{R}_X(\boldsymbol{X}, \boldsymbol{Y}) = \mathbf{A}(\boldsymbol{Y})\boldsymbol{X} + \boldsymbol{K}_X(\boldsymbol{Y}), \tag{27}$$

while the matrix $\mathbf{M}$ is given by (Palenzuela et al. 2009)[8]

$$\mathbf{M}(\boldsymbol{Y}^{*,i}) = \left[\mathbf{I} - a_{ii}\Delta t \mathbf{A}(\boldsymbol{Y}^{*,i})\right]^{-1}, \tag{28}$$

where $\mathbf{I}$ is the identity matrix.

[6] An alternative approach to solve the special relativistic RHD equations in a moderately stiff regime has been considered in 1D Lagrangian simulations by Dumbser, Uuriintsetseg & Zanotti (2012).

[7] Note that the global order of an IMEX scheme does not uniquely determine the number of substages.

[8] We stress that the form of $\mathbf{M}$ given by equation (28) is only valid for the decomposition as done in equation (27).

For each RK substage, $\{\boldsymbol{X}^{(i)}, \boldsymbol{Y}^{(i)}\}$ is computed as described above, and finally the time update is performed as

$$\boldsymbol{\mathcal{U}}^{n+1} = \boldsymbol{\mathcal{U}}^{n} + \Delta t \sum_{i=1}^{\nu} \tilde{\boldsymbol{w}}_i F[\boldsymbol{\mathcal{U}}^{(i)}] + \Delta t \sum_{i=1}^{\nu} \boldsymbol{w}_i R[\boldsymbol{\mathcal{U}}^{(i)}], \tag{29}$$

where $\tilde{\boldsymbol{w}}_i$ and $\boldsymbol{w}_i$ are coefficient vectors. In most of the applications presented in this paper, we have adopted the SSP3(4, 3, 3) (strong stability preserving of order three) IMEX RK scheme. The notation SSP $k(s, \sigma, p)$ is adopted to specify the order of the SSP scheme (k), the number of stages of the implicit scheme (s), the number of stages of the explicit scheme (σ) and the order of the IMEX scheme (p) (Pareschi & Russo 2005). The coefficient tables employed in this paper are listed in Appendix B.

2.2.2 *Specification to radiation hydrodynamics*

Because of the complexity of the GR-RHD equations, isolating the term (or the terms) that are responsible for the stiffness is not a trivial task, although we can certainly say that such terms are contained in the radiation four-force $G^{\alpha}_{\rm r}$. According to the logic of the IMEX scheme just described, we identify $\{\boldsymbol{X}\}$ with the radiation hydrodynamical variables $\{U_{\rm r}, (S_{\rm r})_j\}$ that are affected by stiffness, and $\{\boldsymbol{Y}\}$ with $\{D, S_j, U\}$, that remain unaffected.

As highlighted above, the IMEX scheme requires the stiff source terms $\boldsymbol{R}_X$ to be decomposed according to equation (27). We therefore write the radiation four-force $G^{\alpha}_{\rm r}$ in terms of the conservative variables of the radiation field. To this extent, we rewrite equations (18) and (19) to find the radiation energy density $E_{\rm r}$ and the fluxes $F^{\alpha}_{\rm r}$ in terms of $U_{\rm r}$ and $(S_{\rm r})_i$ as

$$E_{\rm r} = -3\Gamma^2 W \left[2(S_{\rm r})_k v^k + U_{\rm r}(1/\Gamma^2 - 2)\right], \tag{30}$$

$$F^t_{\rm r} = \frac{\Gamma}{\alpha} W \left[-4U_{\rm r}(\Gamma^2 - 1) + (4\Gamma^2 - 1)(S_{\rm r})_k v^k\right], \tag{31}$$

$$(f_{\rm r})_i = \frac{(S_{\rm r})_i}{\Gamma} - \frac{4}{3} E_{\rm r} \Gamma v_i - \alpha (F_{\rm r})^t v_i, \tag{32}$$

where $W = 1/(1 + 2\Gamma^2)$. In this way, and after some simple algebra, we can rewrite the radiation four-force as

$$G^t_{\rm r} = -\frac{\Gamma}{\alpha} \left[\chi^{\rm t} a_r T^4_{\rm fluid} + U_{\rm r}(2\chi^{\rm s}(1 - 3W) - \chi^{\rm t}) + (S_{\rm r})_k v^k (\chi^{\rm t} + \chi^{\rm s}(3W - 2))\right], \tag{33}$$

$$(G_{\rm r})_i = -\chi^{\rm t} a_r T^4_{\rm fluid} v_i \Gamma + \frac{(\chi^{\rm t} + \chi^{\rm s})}{\Gamma}(S_{\rm r})_i + U_{\rm r}\Gamma v_i \left[\chi^{\rm t}(1 - 4W) + 2\chi^{\rm s}(W - 1)\right] + (S_{\rm r})_k v^k \Gamma v_i \left[\chi^{\rm t}(2W - 1) + \chi^{\rm s}(2 - W)\right]. \tag{34}$$

We note that the right-hand sides of equations (33) and (34) do not contain the set of variables $\{\boldsymbol{Y}\}$, while they do contain the conserved variables $\{\boldsymbol{X}\}$, which always appear with a multiplication factor containing either $\chi^{\rm t}$ or $\chi^{\rm s}$. This is an indication that, depending on the values assumed by the opacities, such source terms may become stiff, *but only for the radiation variables*. This means that the vector of sources given by equation (13) will be split in two parts, $\boldsymbol{\mathcal{S}} = \boldsymbol{\mathcal{S}}_e + \boldsymbol{\mathcal{S}}_i$. The first one,

$$\boldsymbol{\mathcal{S}}_e \equiv \sqrt{\mathfrak{s}} \begin{bmatrix} 0 \\ \frac{1}{2}\alpha W^{ik}\partial_j \mathfrak{s}_{ik} + S_i \partial_j \beta^i - U\partial_j \alpha + \alpha (G_{\rm r})_j \\ \frac{1}{2} W^{ik}\beta^j \partial_j \mathfrak{s}_{ik} + W_i{}^j \partial_j \beta^i - S^j \partial_j \alpha + \alpha^2 G^t_{\rm r} \\ \frac{1}{2} R^{ik}_{\rm r} \beta^j \partial_j \mathfrak{s}_{ik} + (R_{\rm r})^j_i \partial_j \beta^i - S^j_{\rm r} \partial_j \alpha \\ \frac{1}{2}\alpha R^{ik}_{\rm r} \partial_j \mathfrak{s}_{ik} + (S_{\rm r})_i \partial_j \beta^i - U_{\rm r} \partial_j \alpha \end{bmatrix}, \tag{35}$$

will be absorbed into the operators F_Y and F_X in equations (21) and (22) because it does not contain stiff terms. The second part, on the other hand, which contains the genuinely stiff terms for the radiation variables $\{\boldsymbol{X}\}$, is

$$\boldsymbol{\mathcal{S}}_i \equiv \sqrt{\mathfrak{s}} \begin{bmatrix} 0 \\ 0 \\ 0 \\ -\alpha^2 G^t_{\rm r} \\ -\alpha (G_{\rm r})_j \end{bmatrix}, \tag{36}$$

and its non-zero components are identified with $\boldsymbol{R}_X(\boldsymbol{X}, \boldsymbol{Y})$ in equation (22). After using equations (33) and (34), it is possible to further decompose $\boldsymbol{R}_X$ as prescribed by equation (27) as

$$\begin{bmatrix} -\alpha^2 G^t_{\rm r} \\ -\alpha (G_{\rm r})_j \end{bmatrix} = \mathbf{A}(\boldsymbol{Y}) \begin{bmatrix} U_{\rm r} \\ (S_{\rm r})_j \end{bmatrix} + \begin{bmatrix} \alpha\Gamma\chi^{\rm t} a_r T^4_{\rm fluid} \\ \alpha\Gamma\chi^{\rm t} a_r T^4_{\rm fluid} v_j \end{bmatrix}, \tag{37}$$

where the coefficients of the matrix $\mathbf{A}(\boldsymbol{Y})$ are specified in Appendix B. The components of the vector $\boldsymbol{K}_X$ (the second term on the right-hand side of equation 37) do not depend on the stiff variables $\boldsymbol{X}$, but only on the temperature $T_{\rm fluid}$. We note that, in the actual implementation

of the IMEX RK scheme, the correction to the implicit variables $\boldsymbol{X}^{(i)}$ dictated by equation (26) is performed when the conversion from the conservative variables $\boldsymbol{\mathcal{U}}$ to the primitive variables is performed.

2.3 Numerical tools

For reasons of flexibility, cross-verification and in view of future projects, we have implemented the GR-RHD equations in their IMEX version in two different numerical codes.

The first one is a modification of the WHISKY code, which implements the GR resistive MHD formalism WHISKYRMHD (Dionysopoulou et al. 2012). We use the numerical methods provided by the original WHISKY code documented in Baiotti et al. (2003) and Giacomazzo & Rezzolla (2007), namely an HLLE approximate Riemann solver and a second-order TVD slope limiter method for the reconstruction of the primitives. The infrastructure as well as the solution of the Einstein equations is provided by the `Cactus` Computational Toolkit (Löffler et al. 2012). The implementation of the GR-RHD equations in WHISKYRMHD required modifications mainly in the sources and the routine which recovers the primitives from the conservative variables. In order to deal with the stiffness of the source terms, we have modified the MoL thorn (part of Einstein Toolkit[9]), by including second- and third-order IMEX RK time integrators.

The second code is based on ECHO (Del Zanna et al. 2007), which provides a numerical platform for the solution of the GR-MHD equations in stationary background space–times.[10] It employs a high-order shock-capturing Godunov scheme with a two-waves HLL Riemann solver, while the spatial reconstruction of the primitive variables can be obtained by linear and non-linear methods. Time integration is possible in either second- or third-order IMEX RK. Previously in Paper I, ECHO had been extended to allow the solution of the non-stiff GR-RHD equations in the optically thick regime.

In both WHISKY and ECHO, our implementation of the stiff GR-RHD equations does not allow for a treatment of the optically *thin* regime. Therefore, all the tests and applications described in this paper are limited to the optically *thick* regime, while we postpone an accurate analysis of the variable Eddington factor approach to a future work.

Finally, we note that the increase of computational cost when changing from an explicit RK of order k to a RK-IMEX of the same order k is approximately given by the ratio of the number of substages required by the IMEX to the number of substages required by the explicit RK. For the SSP3-IMEX scheme, compared to the explicit RK3, such a nominal ratio is given by $5/3 \sim 1.67$ and in both our implementations we have measured an effective factor of $\sim$1.8 increase.

3 VERIFICATION OF THE SCHEME

In Paper I, we had considered a number of shock-tube tests in which non-linear RHD waves propagate. The semi-analytic solution that is used for comparison with the numerical one has been obtained following the strategy of Farris et al. (2008), and it requires the solution of the following system of ordinary differential equations

$$d_x \mathbf{U}(\mathbf{P}) = \mathbf{S}(\mathbf{P}), \tag{38}$$

where

$$\mathbf{P} = \begin{pmatrix} \rho \\ P \\ u^x \\ E_{\rm r} \\ F^x_{\rm r} \end{pmatrix}, \qquad \mathbf{U} = \begin{pmatrix} \rho u^x \\ T^{0x} \\ T^{xx} \\ T^{0x}_{\rm r} \\ T^{xx}_{\rm r} \end{pmatrix}, \qquad \mathbf{S} = \begin{pmatrix} 0 \\ 0 \\ 0 \\ -G^0_{\rm r} \\ -G^x_{\rm r} \end{pmatrix}.$$

U_1, U_2 and U_3 are constant in x, while only $T^{0x}_{\rm r}$ and $T^{xx}_{\rm r}$ need to be solved for. These tests can be used to monitor the ability of the code to deal with the stiff regime, by simply increasing the thermal opacity $\kappa^{\rm t}_g$ (the scattering opacity $\kappa^{\rm s}_g$ is set to zero). When this is done, the semi-analytic solution of the ODE system (38) can be obtained with an ODE solver for stiff systems (Press et al. 1992). The initial states of the two tests that we have considered are reported in Table 1 and are chosen in such a way that the discontinuity front at $x = 0$ remains stationary, namely it is comoving with the Eulerian observer. LTE is assumed at both ends $x = \pm X$, with $X = 20$, and this is obtained by adopting a fictitious value of the radiation constant $a_{\rm rad}$, namely $a_{\rm rad} = E_{{\rm r},L}/T^4_L$, which is then used to compute $E_{{\rm r},R} = a_{\rm rad} T^4_R$ (here the indices L and R indicate the 'left' and 'right' states, respectively). We note that tests No. 1 and 2 in Table 1 are the same as tests No. 3 and 4 in table 1 of Paper I, apart for the value of $\kappa^{\rm t}_g$, which controls the stiffness of the problem. After setting 800 grid points in the x-direction, we have increased the value of $\kappa^{\rm t}_g$ to the maximum value affordable by the numerical scheme, *while keeping the* $\mathcal{C}_{\rm CFL}$ *parameter unchanged and equal to 0.25*. For example, $\kappa^{\rm t}_g$ has been increased from 0.3 to 25.0 in test No. 1, and from 0.08 to 0.7 in test No. 2. Each test is evolved in time until stationarity is reached, and the results are shown in Fig. 1, where the numerical solution is compared to the semi-analytic one in the two cases considered.

[9] The Einstein Toolkit: A Community Computational Infrastructure for Relativistic Astrophysics (cac); http://www.cactuscode.org.
[10] See also Bucciantini & Del Zanna (2011) for a recent extension of ECHO to dynamical space–times within the conformally flat approximation.

Table 1. Description of the initial data – in the shock-tube tests with radiation field. The different columns refer, respectively, to the test considered, the adiabatic index, the radiation constant and the thermal opacity. Also reported are the rest-mass density, pressure, velocity and radiation energy density in the 'left' (L) and 'right' (R) states.

Model	γ	$a_{\rm rad}$	$\kappa_g^{\rm t}$	ρ_L	P_L	u_L^x	$E_{{\rm r},L}$	ρ_R	P_R	u_R^x	$E_{{\rm r},R}$
1	2	1.543×10^{-7}	25	1.0	60.0	10.0	2.0	8.0	2.34×10^{3}	1.25	1.14×10^{3}
2	5/3	1.388×10^{8}	0.7	1.0	6.0×10^{-3}	0.69	0.18	3.65	3.59×10^{-2}	0.189	1.3
3	2	1.543×10^{-7}	1000	1.0	60.0	1.25	2.0	1.0	60.0	1.10	2.0

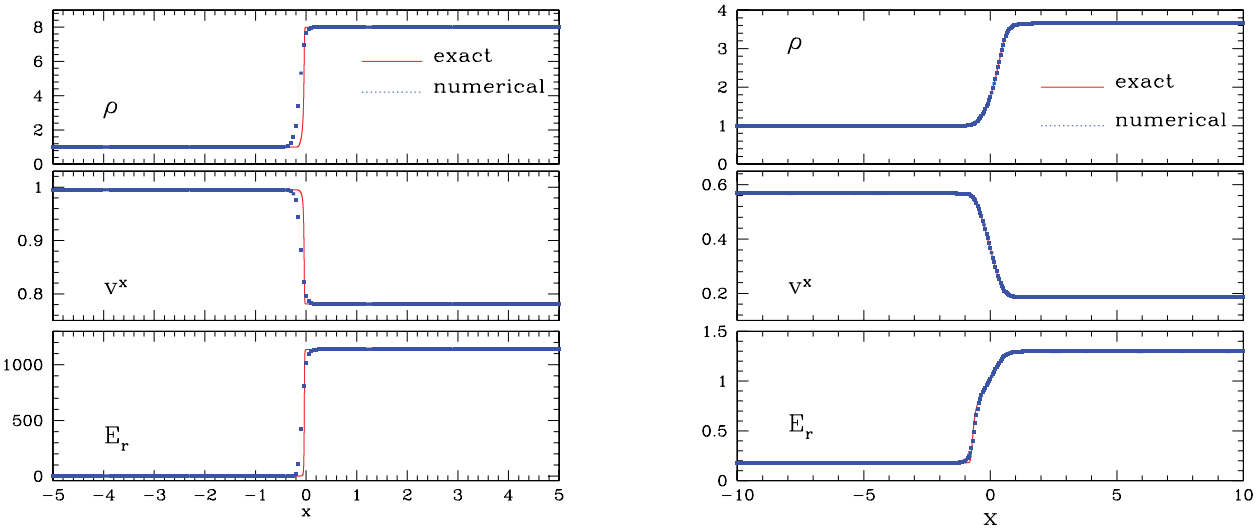

Figure 1. Shock tubes – solution of the test No. 1 (left-hand panel) and No. 2 (right-hand panel). From top to bottom the panels report the rest-mass density, the velocity and the radiation energy density. In both cases 800 grid points have been used with $\mathcal{C}_{\rm CFL} = 0.25$ and RK-IMEX2. The tests are performed with the WHISKY code, employing TVD reconstruction and minmod limiter.

It should also be noted that shock-tube problems do not represent an ideal set-up to highlight the ability of the scheme in handling the stiffness of the source terms, since strong discontinuities are by themselves a challenge for any numerical method. As a result, we have performed an additional and peculiar shock-tube problem, test No. 3, which has equal left and right states, except for the velocity. In this case, two shock waves propagate in the opposite direction, no stationary solution is obtained, but a much higher value of $\kappa_g^{\rm t}$ can be used, namely $\kappa_g^{\rm t} = 1000$. Fig. 2 reports the corresponding solution at time $t = 15$, and also shows the very good agreement between the results obtained with WHISKY and ECHO.

4 SPHERICAL ACCRETION

Having introduced the numerical tools for the treatment of the stiff source terms typical of GR-RHD, we now focus on a problem that has been the subject of several astrophysical analyses, namely spherical accretion on to a black hole. In the first part of this section, we present an additional test of our numerical scheme, brought in the stiff regime by assuming unphysically large cross-sections. On the other hand, in the second part, we choose physical parameters to model the solution by Michel (1972) in an astrophysical context.

Transonic accretion on to a non-rotating black hole in the presence of an isotropic radiation field has been studied in great detail by several research groups over the years. In the optically thick regime, the stationary solution was investigated under different approximations and by focusing on different emission mechanisms by Maraschi, Reina & Treves (1974), Kafka & Mészáros (1976), Vitello (1978), Gillman & Stellingwerf (1980), Flammang (1982) and Nobili, Turolla & Zampieri (1991). The time-dependent solution was considered by Gilden & Wheeler (1980) and Zampieri, Miller & Turolla (1996). The latter, in particular, solved via a Lagrangian code of the radiation transfer equations using the PSTF moment formalism,[11] is truncated at the first two moment equations. Because of the limiting approximations assumed, and in particular because of the lack of Comptonization effects, our analysis should not be regarded as an attempt to improve with respect to the above-mentioned works, but rather as a preliminary study in view of further developments. We also note that multidimensional simulations with an Eulerian code have been recently performed by Fragile et al. (2012) obtaining promising results.

Our initial conditions are given by the fluid spherically symmetric transonic solution of Michel (1972), which is stationary in the absence of a radiation field. The free parameters of the fluid solution are the critical radius $r_{\rm c}$ and the rest-mass density at the critical radius $\rho_{\rm c}$. We choose a black hole with mass $M = 2.5\,{\rm M}_\odot$, while the adiabatic index of the fluid is $\gamma = 4/3$. The initial radiation field is initialized to

[11] The first time-dependent problems adopting the PSTF formalism were presented in Rezzolla & Miller (1994).

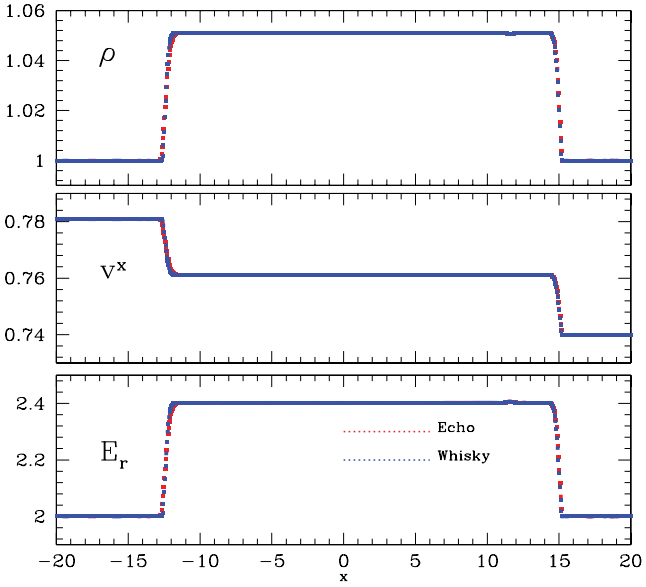

Figure 2. Shock tubes – solution of the test No. 3 at time $t = 15$. From top to bottom, the panels show the rest-mass density, the velocity and the radiation energy density. In both cases, 800 grid points have been used with $\mathcal{C}_{\rm CFL} = 0.25$ and RK-IMEX2. The tests are performed with both the WHISKY and ECHO codes, employing TVD reconstruction and MC limiter.

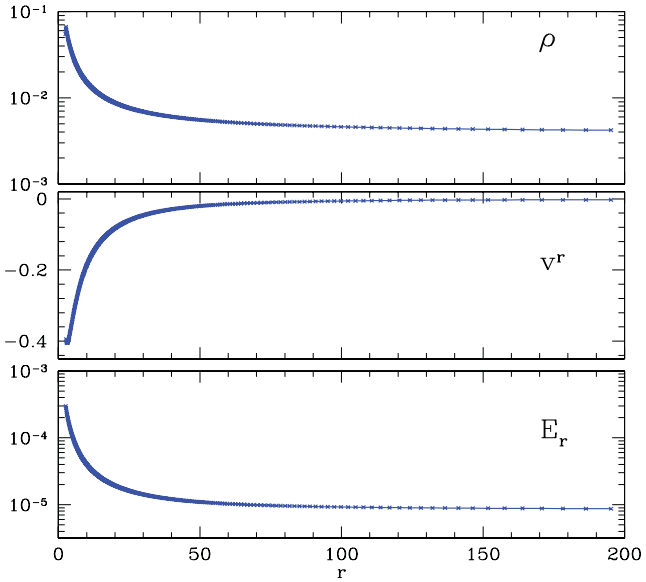

Figure 3. Stiff spherical accretion – numerical solution at time $t = 1000$. From top to bottom the panels report the rest-mass density, the velocity and the radiation energy density. An artificial $\kappa_g^{\rm t} = 1.0 \times 10^{15}$ has been adopted to highlight the ability of the code to treat the stiff regime. $N_{\rm r} = 300$ grid points have been used with $\mathcal{C}_{\rm CFL} = 0.2$, MC reconstruction and SSP3-IMEX.

a negligible energy density, while radiation fluxes are set to zero. As a first test, aimed at showing the ability of the numerical scheme in handling the stiff regime, we have considered an unphysical set-up with $\rho_{\rm c} = 0.02$, $r_{\rm c} = 8.0$, and a high uniform value of the thermal opacity, $\kappa_g^{\rm t} = 10^{15}$. The test is performed in Boyer–Lindquist coordinates with $2.5 < r < 200$ using $N = 300$ radial grid points. The SSP3-IMEX scheme has been adopted, with the MC limiter for the spatial reconstruction. Fig. 3 shows the profiles of the rest-mass density, the radial velocity and the radiation energy density (from top to bottom) at time $t = 1000$. We stress that, if the IMEX scheme is not available, and the evolution is performed through a fully explicit RK scheme, this test can be successfully repeated at the same $\mathcal{C}_{\rm CFL} = 0.2$ only with a value of $\kappa_g^{\rm t} \lesssim 1$.

Having done that, we have concentrated on a sequence of more realistic models, all of them with $\rho_{\rm c} = 9.88 \times 10^{-9}$ cgs, but with different critical radii ($r_{\rm c}$), chosen in the range between 800 and 7000, in order to control the accretion rate. The test is performed in Kerr–Schild coordinates with $1.0 < r < 1000$ using $N = 3200$ radial grid points. The evolution is stopped when stationarity in the $L2$ norms of all of the variables has been reached, which may require a final time as long as $t = 400\,000$ in code units. The scheme employed is the SSP3-IMEX, with MC limiter.

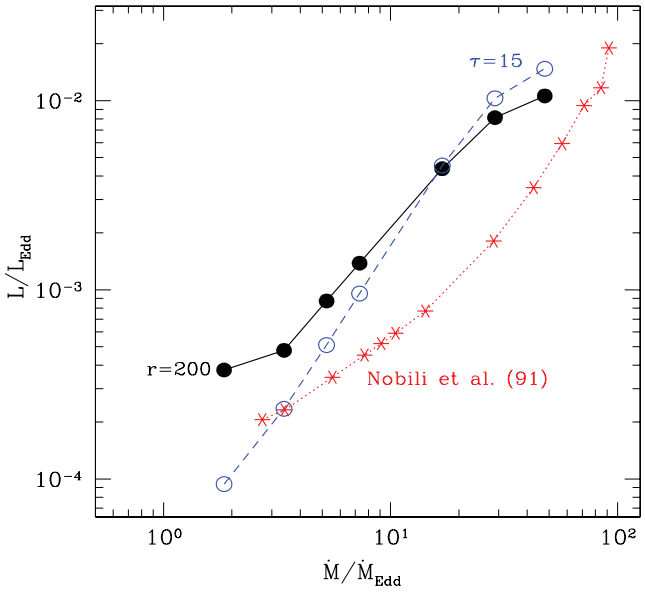

Figure 4. Spherical accretion: luminosity (accretion rate $\dot{M}$) – in Eddington units. Luminosity L was extracted either at constant optical depth τ or at constant radius r. Additionally in red, we show the high-luminosity branch found in Nobili et al. (1991) for comparison.

Special attention has to be paid to the boundary conditions at the outer radial grid point, for which we have followed closely the discussion presented by Nobili et al. (1991). In particular, zeroth-order extrapolation (copy of variables) is adopted for the gas pressure and for the density. This guarantees that the temperature has zero gradient. At the same time we want to make sure that at large radii the radiation field streams radially, namely that $E \propto f^r \propto r^{-2}$. This translates into the condition

$$\frac{\mathrm{d}\ln E}{\mathrm{d}\ln r} = -2, \tag{39}$$

which can be easily implemented. Finally, we fix the accretion rate at the outer boundary to the value possessed by the initial configuration. At the inner radial boundary, on the other hand, zeroth-order extrapolation is adopted for all of the variables. The evolution is performed considering both the contribution of the bremsstrahlung opacity and of the Thomson scattering opacity for electrons. We note that during the evolution the radiation flux remains typically two orders of magnitude smaller than the radiation energy, thus maintaining the code in the physical regime for which it was designed. After an initial relaxation, the system converges to a different stationary configuration characterized by a non-zero radiation flux. The solution is optically thick in all the models for $r \leq 100$, while it becomes marginally optically thick at large radii. From the radiation flux we compute the luminosity as $L = 4\pi r^2 f^r$.

Fig. 4 reports the results of our simulation tests in the diagram $(\dot{M}/\dot{M}_{\rm Edd}, L/L_{\rm Edd})$, where the luminosity is computed at $r = 200$. Although our data resemble the high-luminosity branch reported in fig. 1 of Nobili et al. (1991), a close comparison with their results is not really possible, since Comptonization, bound–bound transitions and free–bound transitions are not taken into account in our analysis. In particular, the absence of pre-heating effects does not allow us to verify the onset of strong thermal instabilities producing hydrodynamic shock waves that propagate outward, as reported by Zampieri et al. (1996). In spite of this, the test we have performed is very relevant. In fact, by using an entirely different procedure with respect to Nobili et al. (1991) and Zampieri et al. (1996), it confirms the existence of a high-luminosity branch in the diagram $(\dot{M}/\dot{M}_{\rm Edd}, L/L_{\rm Edd})$, which corresponds to the optically thick regime. A more extended analysis of this problem, by including additional contributions to the opacity, a treatment of the Comptonization and the effect of a spinning black hole will be the focus of a separate and dedicated work.

5 BONDI–HOYLE–LYTTLETON ACCRETION

This section deals with the application of our new scheme to simple astrophysical models departing from spherical symmetry. We revisit the BHL accretion flow that we already described in some detail in Paper I, and whose initial conditions are briefly summarized in Section 5.1. After showing consistency with the non-stiff solver, we illustrate the effectiveness of the IMEX by treating models of low temperature, which is the key parameter responsible for numerical difficulty. Only now, it becomes feasible to treat astrophysical temperatures that are few orders of magnitude lower than in Paper I and as astrophysically realistic as our approach can allow at this stage (cf. conclusion for more discussion). Having thus reached the limits imposed by the physical assumptions of the current treatment, we now analyse the dynamics of the fluid, the occurrence of shocks and the possible observational quantities, with particular attention to the computation of the luminosity. We stress that it is not our intention to perform a systematic analysis of the full parameter space.

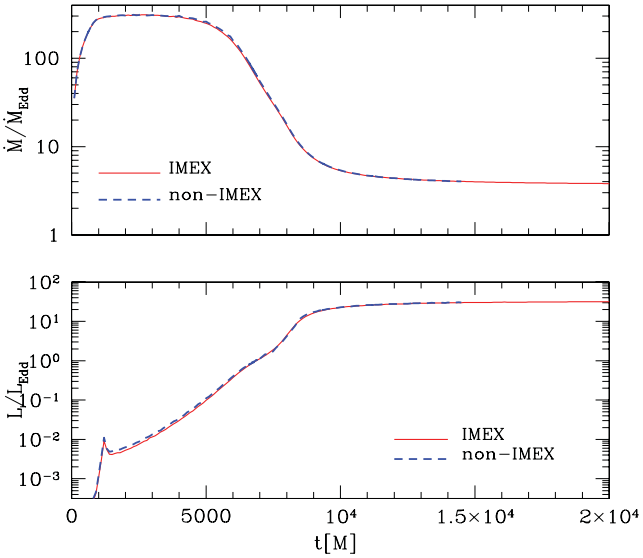

Figure 5. Consistency test of the new IMEX scheme – time evolution of a perturbed BHL model with $v_{\rm inf} = 0.18$ and $c_{s,\infty} = 0.07$ (model `p.V18.cs07` of Paper I) with the IMEX (solid line) and with the non-IMEX version of the code (dashed line). The lower panel shows the light curve, whereas the accretion rate is plotted in the top panel. All curves are shown in Eddington units.

5.1 Initial conditions for the BHL accretion flow

We perform 2D numerical simulations of a BHL accretion flow (Hoyle & Lyttleton 1939; Bondi & Hoyle 1944) on to a Schwarzschild black hole of Galactic size with $M_{\rm BH} = 3.6 \times 10^6\,{\rm M}_\odot$. The initial conditions considered are similar to those adopted in Paper I, with a velocity field that is specified in terms of an asymptotic velocity v_∞ (Font & Ibáñez 1998)

$$v^r = \sqrt{\mathfrak{g}^{rr}}\, v_\infty \cos\phi, \tag{40}$$

$$v^\phi = -\sqrt{\mathfrak{g}^{\phi\phi}}\, v_\infty \sin\phi, \tag{41}$$

where $\mathfrak{g}^{ij}$ are the components of the three-metric and ϕ is the azimuthal angle in Boyer–Lindquist coordinates. The radiation field is initialized to a uniform and small energy density $E_{\rm r}$, such that the radiation temperature $T_{\rm rad} = (E_{\rm r}/a_{\rm rad})^{1/4} \approx 1.5 \times 10^5$ K. Additional free parameters are the asymptotic sound speed $c_{s,\infty}$, and the asymptotic pressure, from which the asymptotic rest-mass density ρ_∞ follows directly. The resulting configuration relaxes to a different and stationary one, on a time-scale that depends on the parameters chosen. Keeping to nomenclature of Paper I, we encode the two parameters $v_{\infty_{0.1}}$ and $c_{s,\infty_{0.1}}$[12] and a prefix denoting perturbation (if applicable) in our naming scheme as `---.v`$v_{\infty_{0.1}}$`.c`$_{s,\infty_{0.1}}$. The adiabatic index of the fluid is $\gamma = 5/3$.

The computational grid consists of $N_{\rm r} \times N_\phi$ numerical cells in the radial and angular directions, respectively, covering a computational domain extending from $r_{\rm min} = 2.1\,M$ to $r_{\rm max} = 200\,M$ and from $\phi_{\rm min} = 0$ to $\phi_{\rm max} = 2\pi$. For our fiducial simulation we have chosen $N_{\rm r} = 1536$ and $N_\phi = 300$, but have also verified that the results are not sensitive to the resolution used or to the location of the outer boundary.

5.2 Consistency test

Before going to new models, we first carried out a consistency test using a representative model with Mach number $\mathcal{M}_\infty = 2.57$ (model `p.V18.cs07` of Paper I) and reproducing it with the present new IMEX version of ECHO. As shown in Fig. 5, the IMEX version reproduces the light curves and the accretion rates obtained with the purely explicit version of the code. Moreover, by using the IMEX scheme, it is now possible to extend the evolution to later times, whereas the previous version of the code required reducing the $\mathcal{C}_{\rm CFL}$ to values smaller than 0.01, making such long evolutions practically unfeasible. This test confirms that the new scheme is verified also in a non-trivial 2D application and that the use of the IMEX offers clear advantages in terms of computational resources.

5.3 Results

In the following we examine the behaviour of three models, with two different initial sound speeds $c_{s,\infty}$ and the same asymptotic velocity v_∞. The prefix `sp` is used to denote 'strongly perturbed' which means that the initial asymptotic pressure is lowered by two orders of magnitude with respect to the equilibrium value. This is done with the main purpose of producing models with even lower temperatures.

[12] Here, subscripts 0.1 denote the normalization in units of $0.1c$, so $v_{\infty_{0.1}} = v_\infty/(0.1c)$. Therefore, the model `V07.cs03` has $v_\infty = 0.07$ and $c_{s,\infty} = 0.03$.

Measured physical quantities. In addition to the primitive variables provided by the code, we calculate several physical quantities: the accretion rate in Eddington units, $\dot{M}$, the luminosity in Eddington units, L, the radiation equivalent temperature, $T_{\rm rad} = (E_{\rm r}/a_{\rm rad})^{1/4}$, the fluid temperature, $T_{\rm fluid}$, the effective adiabatic index, $\gamma_{\rm eff}$:

$$\gamma_{\rm eff} = \frac{5/2 + 20q + 16q^2}{(3/2 + 12q)(1+q)} \quad \text{with} \quad q = \mathcal{P}_{\rm r}/P, \tag{42}$$

and the local Mach number $\mathcal{M}$:

$$\mathcal{M} = \frac{\Gamma\sqrt{v_i v^i}}{\Gamma_{c_{\rm s}} c_{\rm s}} \quad \text{with} \quad c_{\rm s} = \sqrt{\frac{\gamma P}{h\rho}} = \sqrt{\frac{\gamma P}{\rho + \frac{\gamma}{\gamma-1}P}}\,. \tag{43}$$

Moreover, as discussed in Paper I, we define an effective BHL luminosity efficiency $\eta_{\mathcal{BHL}}$ that takes into account the injected energy at infinity as

$$\eta_{\mathcal{BHL}} = \frac{L}{\dot{M}_{\rm acc}c^2 + \frac{1}{2}\dot{M}_\infty v_\infty^2}\,. \tag{44}$$

We measure several quantities Q as volume-weighted averages over all grid elements i, thus defining the pointy brackets as

$$\langle Q \rangle = \frac{1}{\sum_i^N r_i \mathrm{d}r_i \mathrm{d}\phi_i} \left(\sum_i^N Q_i\, r_i \mathrm{d}r_i \mathrm{d}\phi_i \right)\,. \tag{45}$$

The rate of entropy generation is measured according to equation (A5), which is an appropriate approximation for a coupled photon fluid plasma in a quasi-stationarity state. When we extract the luminosity, we choose a surface of constant optical depth $\tau \gtrsim 10$. We argue that this is reasonable because only if $\tau \gg 1$ the system is still in a regime where the approximation with the diffusion limit is valid. This is also realistic, when thinking of actual observations, where measurements are taken at constant[13] τ. For a discussion of how the luminosity estimates change with respect to Paper I, see Appendix A. Suffice it to say that this luminosity is a tracer of the outwards radial fluxes and that different possible extractions agree within the current error bars.

The optical depth τ is computed in post-processing as in Paper I

$$\tau = \int_0^L (\chi^{\rm t} + \chi^{\rm s})\,\mathrm{d}s, \tag{46}$$

where we have assumed a constant characteristic length scale $L = 10$. All other quantities are standard and reported in cgs units. Selected results are shown in Figs 6–8 and summarized in Table 2.

BHL dynamics dominated by radiation quantities. First of all, we note that the qualitative dynamics of all BHL models is the same as described in Paper I and can be summarized as follows (see also Petrich et al. 1989; Font & Ibáñez 1998; Dönmez, Zanotti & Rezzolla 2011 for the hydrodynamics case and Penner 2011 for the MHD one). Initially, a narrow, hot shock cone forms downstream of the accretor and the plasma is fluid-pressure dominated. Progressively, the radiation field builds up strength until the radiation pressure becomes similar to the fluid pressure. At this point, the shock cone becomes unstable, oscillating from one side of the accretor to the other, until it finally reverses into the upstream domain as a bow shock. From now on the radiation pressure exceeds the fluid pressure, the effective adiabatic index approaches the value ∼4/3 and, at the same time, the density (and correspondingly the optical depth) decreases in most parts of the numerical domain. After the upstream shock has moved out of the numerical domain and expelled a significant amount of mass, a new, low-density equilibrium is formed in which there is a smaller shock cone in the downstream region (this is illustrated well in fig. 3 of Paper I, which shows a comparison of BHL flows with and without the radiation field).

The central improvement over Paper I is shown in Fig. 6, where the 2D maps of the optical depth (left) and of the fluid temperature (right) are shown for two different models, both of them at the final quasi-stationary state. The top panels, in particular, show that for the strongly perturbed model `sp.V07.cs03` large parts of the upstream region settle down to temperatures of the order of $T_{\rm fluid} \lesssim 10^6$ K, a value which could not be reached before due to the stiffness of the equations. The corresponding unperturbed model, `V07.cs03`, shown in the bottom panels, has upstream temperatures as high as $T_{\rm fluid} \lesssim 5 \times 10^9$ K, while both of the models have significantly high optical thickness. It is important to note that at this stage of the evolution, namely after the 'reversal' of the shock cone, the effective adiabatic index of all three models is very close to $\gamma_{\rm eff} \sim 4/3$, and therefore behaving like an effective photon fluid.

Additional understanding of the thermodynamics of the models is achieved if we look at the time evolution of the averaged fluid and averaged radiation temperatures, which are plotted in Fig. 7. There are three points worth noting. First of all, for each model, the two temperatures $T_{\rm rad}$ and $T_{\rm fluid}$ differ by many orders of magnitude, suggesting that, at least globally, there is a strong deviation from thermal equilibrium within the fluid. Secondly, the fluid temperatures of the models `sp.V07.cs03` and `V07.cs03` are also significantly different, in spite of the dynamics being very similar (this is discussed in the next section). Finally, $T_{\rm rad}$ shows a smooth evolution, whereas $T_{\rm fluid}$ exhibits a strong dip, reaches a minimum and heats up again afterwards. When the large size and hot ($T_{\rm fluid} \gg 10^{10}$ K) shock cone reverses, the density downstream of the accretor becomes small, yet the pressure remains high. A smaller size high-temperature shock cone forms in the downstream region, as visible in the right-hand panels of Fig. 6, with $T_{\rm fluid}$ average being dominated by the high values within the shock cone.

[13] In the case of stars, for instance, this is usually taken as $\tau \sim 2/3$.

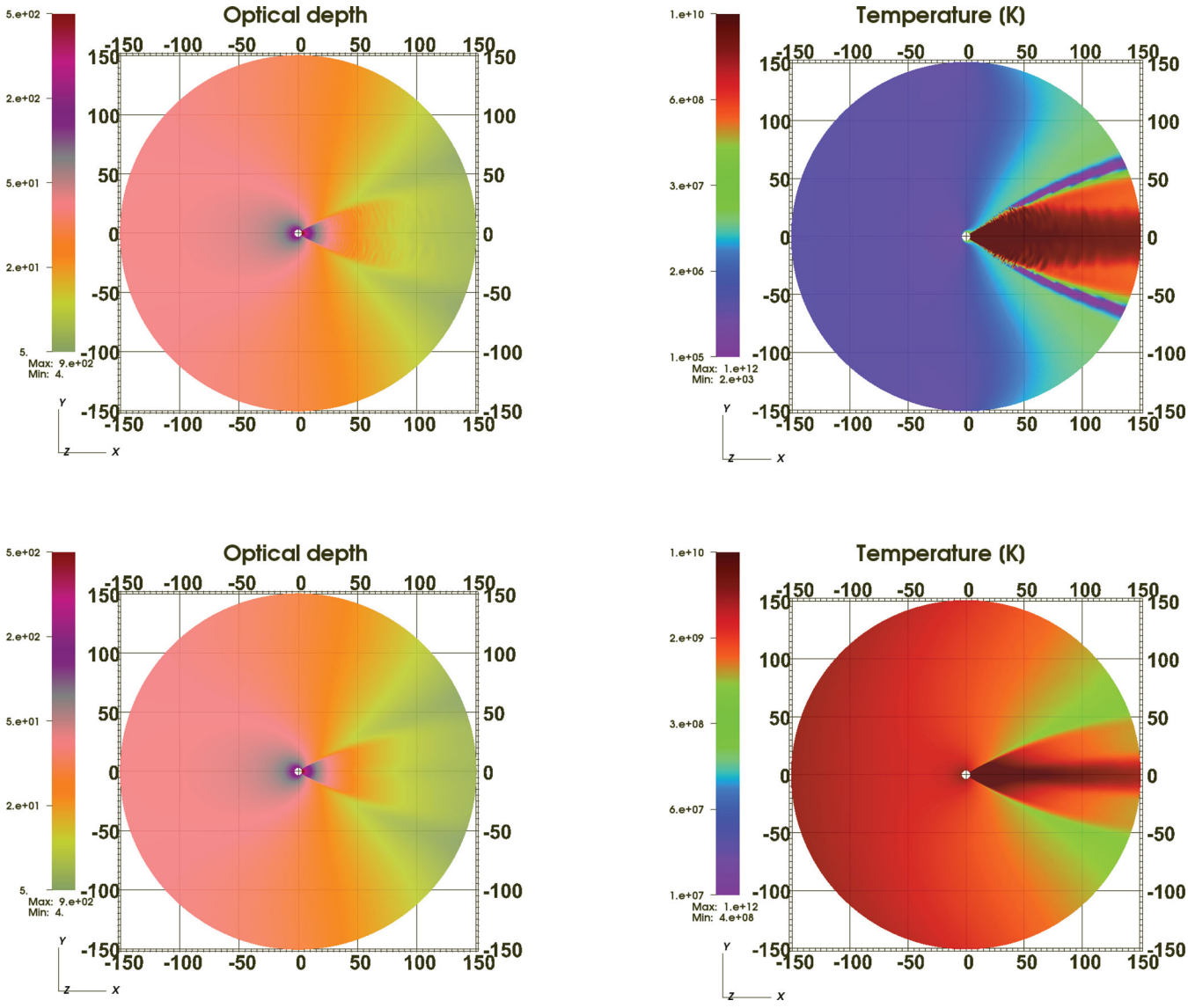

Figure 6. 2D optical depth and fluid temperature of perturbed model `sp.V07.cs03` and unperturbed model `V07.cs03` – both models are shown at a stationary state: $t = 7.71 \times 10^4\, M$ for model `sp.V07.cs03` (top) and $t = 5.98 \times 10^4\, M$ for model `V07.cs03` (bottom).

Thus, the fluid behaves like an effective photon fluid of temperature $T_{\rm rad} \lesssim 10^6$ K, but in the shock cone no thermalization is possible and the fluid temperature vastly exceeds the radiation temperature.

In order to corroborate this description, we measure the entropy generation rate $\nabla_\nu S^\nu$ as an effective tracer of dissipative processes (see Appendix A). The entropy generation rate (Fig. 8 for the two models `V07.cs03` and `sp.V07.cs03`) is maximum in the shocked region downstream of the accretor, where the fluid is very far from thermalization, even though the dynamics is otherwise stationary. Only in the upstream regions where $\nabla_\nu S^\nu$ is very small (cf. the white region of Fig. 8) are the two temperatures $T_{\rm rad}$ and $T_{\rm fluid}$ similar.

To further illustrate the effects of radiation-induced dynamics, we measure two crucial parameters of accretion flows, namely the luminosity and the accretion rate, both of them reported in Eddington units. The computation is performed by directly integrating the escaping radiation fluxes f^r (equation A7), and the infalling mass fluxes at the innermost grid point, respectively. We plot the time evolution of the luminosity and accretion rate, respectively, on the left- and right-hand panels of Fig. 9 for all three models. The important aspects of this figure are that (i) there is a transient peak in the luminosity evolution, corresponding to the point in the dynamics where the shock cone is momentarily dissipated away; (ii) the final luminosity is sub-Eddington for all cases; (iii) the luminosities of the models `sp.V07.cs03` and `V07.cs03` converge towards the same value; and (iv) the higher sound speed (correspondingly the lower asymptotic Mach number $\mathcal{M}_\infty$) of `sp.V07.cs05` leads to smaller luminosity. On the other hand, the corresponding accretion rates are substantially super-Eddington, with final values of $\dot{M}/\dot{M}_{\rm Edd}$ in the range [62, 135], and confirming the advection-dominated nature of BHL accretion flows. The relaxed luminosity efficiency $\eta_{\mathcal{BHL}}$ of the models together with all radiation quantities are listed in Table 2.

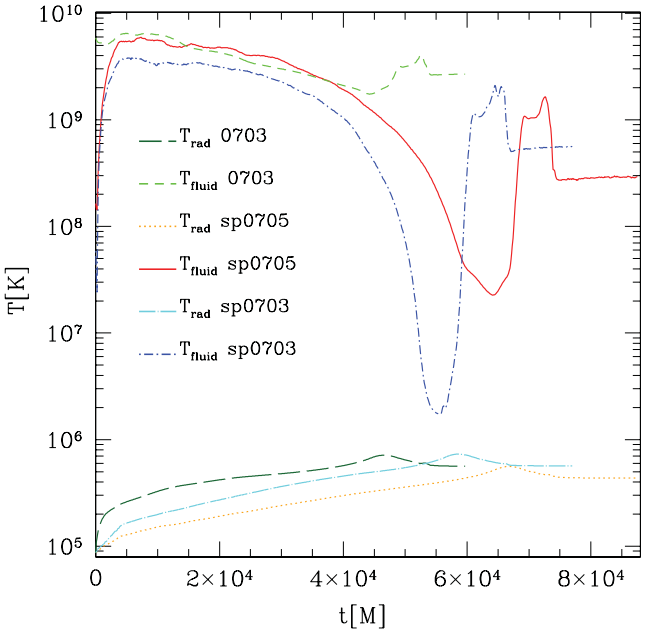

Figure 7. Comparison of fluid and radiation temperatures – volume-weighted averages according to equation (45) for all three BHL models `sp.V07.cs05`, `sp.V07.cs03` and `V07.cs03` as a function of time. Temperatures are given in kelvin.

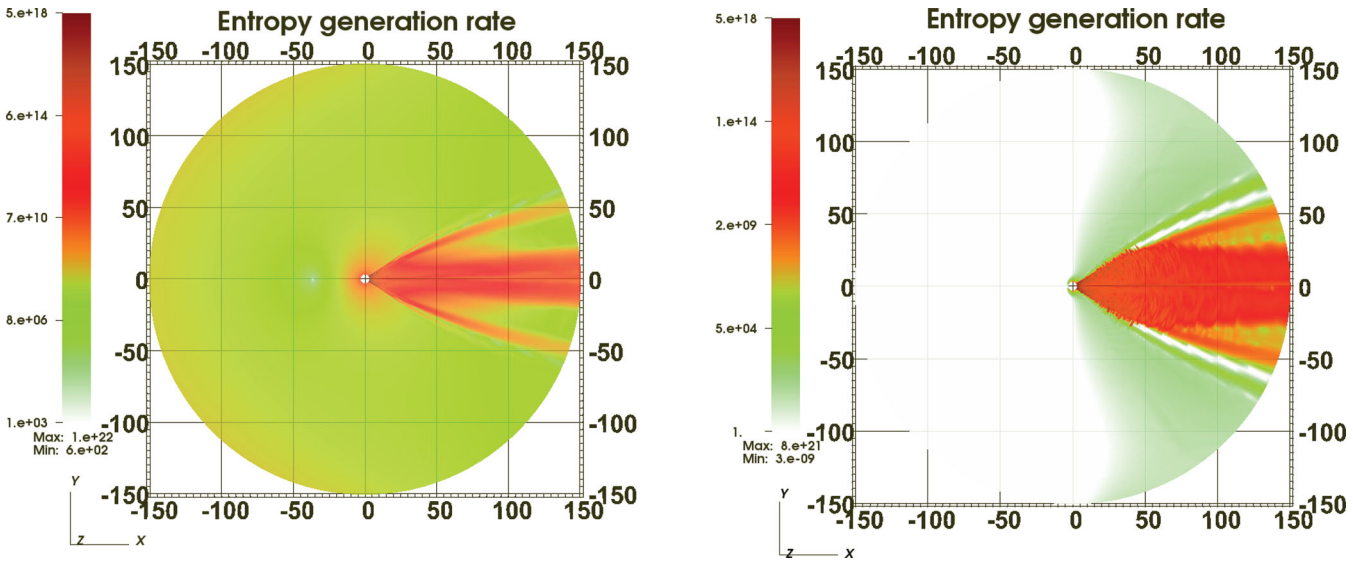

Figure 8. 2D entropy generation rates for `V07.cs03` and `sp.V07.cs03` – distribution map of $\nabla_\nu S^\nu$ for model `V07.cs03` (left-hand panel) at time $t = 5.98 \times 10^4\,M$ and for model `sp.V07.cs03` (right-hand panel) at time $t = 7.71 \times 10^4\,M$.

The role of fluid temperature. It is interesting to note that the strongly perturbed model `sp.V07.cs03` converges towards a final state that is very similar to that of its unperturbed counterpart `V07.cs03`. This is observed in the accretion rate, $\dot{M}$, plotted in the right-hand panel of Fig. 9, in the luminosity, in the radiative efficiency, η (cf. Fig. 10), in the optical depth, τ (cf. Fig. 6), and in the radiation temperature, $T_{\rm rad}$ (cf. Fig. 7), of these two models.

This effect remained obscured in Paper I, due to the fact that the previous criterion for the luminosity extraction was spuriously affected by boundary effects.[14]

While the radiation quantities converge for the two models `sp.V07.cs03` and `V07.cs03`, the quantities more directly related to the fluid properties do not. For example, the fluid temperature, the Mach number and the entropy generation are neither qualitatively and certainly not

[14] See discussion in Appendix A.

Table 2. Representative quantities of the considered models after a quasi-stationary state has been reached. The columns represent the model name, the average radiation temperature, the average effective adiabatic index, the accretion rate, the luminosity and the radiative efficiency, all of them computed after a quasi-stationarity state had been reached. See the text for definition of these quantities.

Name	$\langle T_{\rm rad}\rangle$ (K)	$\langle\gamma_{\rm eff}\rangle$	$\dot{M}/\dot{M}_{\rm Edd}$	$L/L_{\rm Edd}$	$\eta_{\mathcal{BH}}$
`V07.cs03`	5.6×10^5	1.333	132	0.939	6.9×10^{-3}
`sp.V07.cs03`	5.6×10^5	1.334	135	0.943	6.8×10^{-3}
`sp.V07.cs05`	4.3×10^5	1.333	62	0.484	9.0×10^{-3}

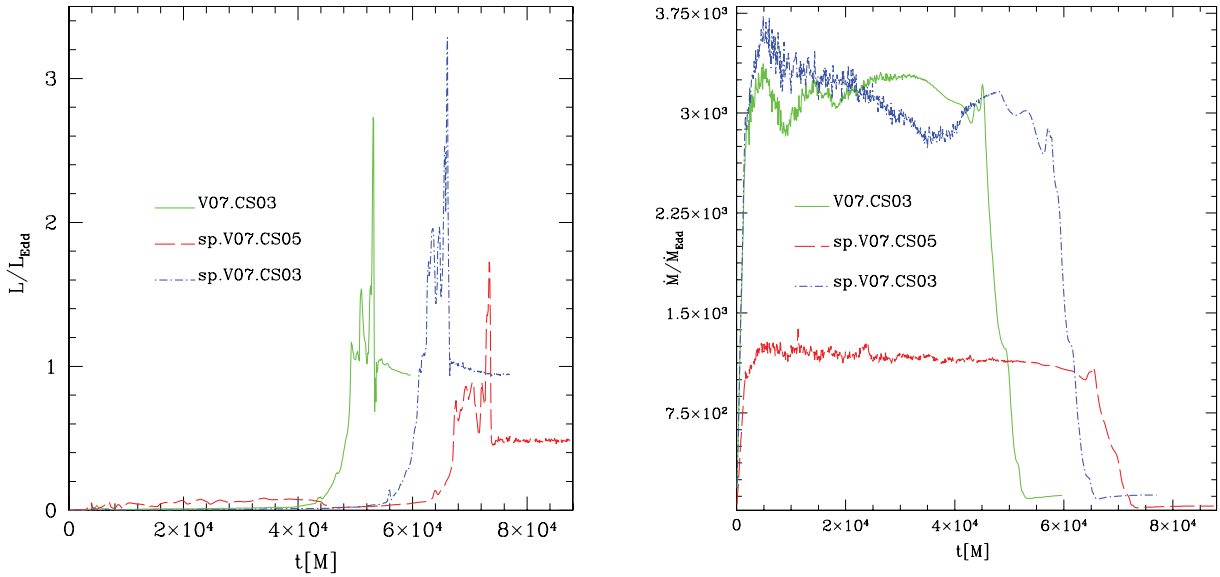

Figure 9. Time evolution of perturbed BHL models `sp.V07.cs05`, `sp.V07.cs03` and `V07.cs03` – left-hand panel: luminosity L extracted at constant optical depth $\tau \geq 10$; right-hand panel: accretion rate $\dot{M}$ as a function of time in Eddington units.

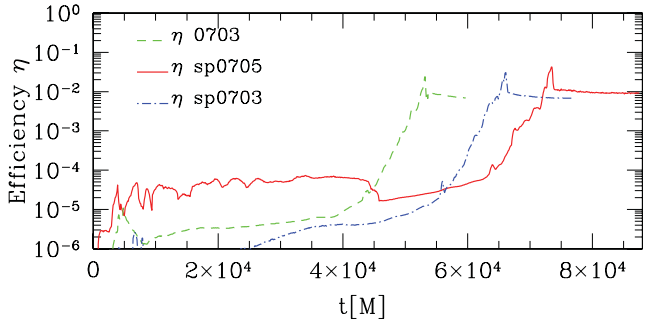

Figure 10. Radiative efficiency – comparison of the radiative efficiency $\eta_{\mathcal{BHL}}$ as a function of time.

quantitatively the same. In addition, the radiation-dominated regime is reached at earlier times for `V07.cs03` as it has higher $T_{\rm fluid}$ and thus higher thermal conductivity (cf. Appendix A).

From the consideration above, it stands to reason that the radiation temperature and the matter density (conversely, the optical depth) are the quantities affecting the dynamics most. This means that bremsstrahlung cannot be a dominant process, since it is a temperature-dependent radiation interaction. This is confirmed by the fact that, when looking at the respective opacities, Thomson scattering dominates over bremsstrahlung by several orders of magnitude. We also note that in some portions of the grid, the discrepancy between $T_{\rm fluid}$ and $T_{\rm rad}$ is very large, implying that the assumption of LTE is not valid there (cf. the red region of Fig. 8). This is consistent with the fact that full thermalization in general is very hard to accomplish in dynamical environments of moderate density.

Further comments. We had already pointed out in Paper I that models with initial high Mach number, $\mathcal{M}_\infty$, are characterized by a luminosity that is dominated by the emission at the shock front, rather than by accretion-powered luminosity. This is also confirmed by the relative comparison between `sp.V07.cs03` and `sp.V07.cs05`, the former having a larger Mach number and a higher luminosity (the left-hand panel of Fig. 9).

Finally, we would like to comment about what has been dubbed the 'flip-flop' instability in BHL accretion flows, and whose physical nature is still a matter of debate (Foglizzo, Galletti & Ruffert 2005). While we do not see this instability in our models (neither in Paper I nor in the present), we have observed that during the 'shock-reversal' strong, although transient, oscillations in the shock cone can appear. However, we suspect that this effect can be partly attributed to the numerics, since the use of the IMEX in combination with a higher order RK (of the order of three instead of two) alters the behaviour of this oscillation slightly. An extended analysis through 3D simulations would be needed to establish the potential relation of this oscillatory behaviour with the eventual development of the flip-flop instability.

6 CONCLUDING REMARKS

In this paper, we have revisited the optically thick, thermal radiation transfer in GR. First, we addressed the numerical problem of stiff source terms; proposed a numerical treatment, implemented and verified it. As we chose an IMEX RK scheme, we needed to isolate the principal stiff parameters, which were found to be the (density-weighted) opacities. After applying the new IMEX method to the 1D problem of spherical accretion, we compared our results with those obtained earlier by Nobili et al. (1991) and found good agreement. In this spherical, stationary scenario the current formulation of the GR-RHD equations is fully applicable as long as the solution remains optically thick. We remark that there is not a unique stiffness threshold, valid for any physical scenario, at which the purely explicit scheme fails and the IMEX becomes necessary. In the case of a purely explicit RK scheme, when the source terms become stiff, it is possible to a certain extent to lower the $\mathcal{C}_{\rm CFL}$ factor and obtain a stable evolution. However, the stiffness parameter can become very large, so the time step becomes very tiny. That is of course inefficient, and resorting to a stiff solver is the only way out. In general, if a problem can be solved with a purely explicit RK scheme, this is to be preferred as the latter is CPU-faster. However, we believe that most non-trivial radiation applications will exhibit stiffness and lead to code crashes with standard explicit RK schemes.

We then revisited the BHL accretion in 2D for an astrophysical, dynamical problem. Here, we could show the following.

(i) The IMEX scheme allows us to evolve models with realistic choice of parameters, of the order of $T \sim 10^6$ K.

(ii) The dynamics of the flow are significantly affected by the radiation pressure, yielding super-Eddington accretion rates in the range $\dot{M} \sim [62, 135]\dot{M}_{\rm Edd}$ and Eddington-limited luminosities.

(iii) The fluid and the radiation depart strongly from thermal equilibrium in shocked regions, particularly in the shock cone downstream of the accretor.

Our analysis has substantially benefited from the ability of our scheme to treat stiff source terms. However, we should also state a few words of caution as to the current shortcomings and necessary future improvements of our scheme.

(i) The optically thin regime cannot be treated yet, and further steps are required to incorporate the variable-Eddington factor approach.

(ii) Temperatures of the order of $T < 10^5$ K, as they appear in small regions of the domain, require the inclusion of bound–free opacities, which are currently neglected.

(iii) The only dissipative mechanism is currently thermal conductivity. Other types of viscosity such as an effective viscosity related to magnetic turbulence would be beneficial. Coupling the current equations to MHD represents another direction of future research.

(iv) Since we currently cannot extract the luminosity in regions where the optical depth is low, we must trace a geometrical surface of constant $\tau \geq 1$. However, it remains an uncertainty as to where such a surface should be placed, and the computed luminosities are therefore affected by at least one order of magnitude uncertainty.

Even in the presence of these limitations, our analysis may become relevant for the study of merging supermassive black hole binaries, which have been attracting a lot of interest for the possible joint measure of electromagnetic and gravitational wave signals (in the context of multimessenger astronomy). Neglecting the back reaction of radiation on to matter, Farris, Liu & Shapiro (2010) already considered the BHL solution in a binary system, finding that luminosities as high as 10^{43} erg s^{-1} can be obtained in a hot gas cloud of temperatures $T \sim 10^6$ K. Such estimates are compatible with our calculations, but a dedicated work will be presented in the future.

ACKNOWLEDGMENTS

CR wishes to thank Nico Budewitz for his helpfulness in HPC support and Aaryn Tonita for his help with the HDF5 I/O. DA thanks E. Schnetter for his guidance during the implementation of the RKIMEX method in the MoL thorn. We are grateful to the anonymous referee whose comments helped improve the clarity of the manuscript. We express our gratitude to Luca Zampieri for providing us with the data shown in Fig. 4. The simulations were performed at the *datura* cluster of the AEI and at SuperMUC at the LRZ München. This work was funded in part by the SFB Transregio 7 of the DFG. CR acknowledges funding by the 'International Max Planck Research School'. OZ acknowledges funding by the European Union's Seventh Framework Programme (FP7/2007–2013) under the research project *STiMulUs*, ERC Grant agreement no. 278267.

REFERENCES

Alic D., Moesta P., Rezzolla L., Zanotti O., Jaramillo J. L., 2012, ApJ, 754, 36
Arnowitt R., Deser S., Misner C. W., 1962, in Witten L., ed., Gravitation: An Introduction to Current Research. Wiley, New York, p. 227
Baiotti L., Hawke I., Montero P., Rezzolla L., 2003, in Capuzzo-Dolcetta R., ed., Computational Astrophysics in Italy: Methods and Tools, Vol. 1. MSAIt, Trieste, p. 210
Bondi H., Hoyle F., 1944, MNRAS, 104, 273
Bucciantini N., Del Zanna L., 2011, A&A, 528, A101
Bucciantini N., Del Zanna L., 2012, ArXiv e-prints (arXiv:1205.2951)
Del Zanna L., Zanotti O., Bucciantini N., Londrillo P., 2007, A&A, 473, 11
Dionysopoulou K., Alic D., Palenzuela C., Rezzolla L., Giacomazzo B., 2012, Phys. Rev. D, submitted (arXiv:1208.3487)
Dönmez O., Zanotti O., Rezzolla L., 2011, MNRAS, 412, 1659
Dumbser M., Uuriintsetseg A., Zanotti O., 2012, Commun. Comput. Phys., submitted
Eckart C., 1940, Phys. Rev., 58, 919
Farris B. D., Li T. K., Liu Y. T., Shapiro S. L., 2008, Phys. Rev. D, 78, 024023
Farris B. D., Liu Y. T., Shapiro S. L., 2010, Phys. Rev. D, 81, 084008
Flammang R. A., 1982, MNRAS, 199, 833
Foglizzo T., Galletti P., Ruffert M., 2005, A&A, 435, 397
Font J. A., Ibáñez J. M., 1998, ApJ, 494, 297
Fragile P. C., Gillespie A., Monahan T., Rodriguez M., Anninos P., 2012, ApJ, 201, 9
Giacomazzo B., Rezzolla L., 2007, Classical Quantum Gravity, 24, S235
Gilden D. L., Wheeler J. C., 1980, ApJ, 239, 705
Gillman A. W., Stellingwerf R. F., 1980, ApJ, 240, 235
Hadrava P., Čechura J., 2012, A&A, 542, A42
Hoyle F., Lyttleton R. A., 1939, Proc. Cambridge Philos. Soc., 35, 405
Hsieh S., Spiegel E. A., 1976, ApJ, 207, 244
Israel W., 1976, Ann. Phys., 100, 310
Kafka P., Mészáros P., 1976, Gen. Relativ. Gravitation, 7, 841
Lentz E. J., Mezzacappa A., Bronson Messer O. E., Liebendörfer M., Hix W. R., Bruenn S. W., 2012, ApJ, 747, 73
Levermore C. D., 1984, J. Quant. Spectrosc. Radiat. Transfer, 31, 149
Löffler F. et al., 2012, Classical Quantum Gravity, 29, 115001
Maraschi L., Reina C., Treves A., 1974, A&A, 35, 389
Michel F. C., 1972, Ap&SS, 15, 153
Mihalas D., Mihalas B., 1984, Foundations of Radiation Hydrodynamics. Oxford Univ. Press, New York
Nobili L., Turolla R., Zampieri L., 1991, ApJ, 383, 250
Palenzuela C., Lehner L., Reula O., Rezzolla L., 2009, MNRAS, 394, 1727
Pareschi L., Russo G., 2005, J. Sci. Comput., 25, 129
Penner A. J., 2011, MNRAS, 414, 1467
Petrich L. I., Shapiro S. L., Stark R. F., Teukolsky S. A., 1989, ApJ, 336, 313
Pfeiffer H. P., 2012, Classical Quantum Gravity, 29, 124004
Pomraning G. C., 1973, The Equations of Radiation Hydrodynamics. Pergamon Press, Oxford
Press W. H., Flannery B. P., Teukolsky S. A., Vetterling W. T., 1992, Numerical Recipes, 2nd edn. Cambridge Univ. Press, New York
Rezzolla L., Miller J. C., 1994, Classical Quantum Gravity, 11, 1815
Schwartz R. A., 1967, Ann. Phys., 43, 42
Schweizer M. A., 1988, Ann. Phys., 183, 80
Shibata M., Kiuchi K., Sekiguchi Y., Suwa Y., 2011, Prog. Theor. Phys., 125, 1255
Thorne K. S., 1981, MNRAS, 194, 439
Vitello P. A. J., 1978, ApJ, 225, 694
Zampieri L., Miller J. C., Turolla R., 1996, MNRAS, 281, 1183
Zanotti O., Roedig C., Rezzolla L., Del Zanna L., 2011, MNRAS, 417, 2899 (Paper I)

APPENDIX A: ENTROPY GENERATION RATE AND LUMINOSITY COMPUTATION

In the framework of Eckart's formulation of relativistic standard irreversible thermodynamics (Eckart 1940), the entropy current is given by

$$\mathcal{S}^{\mu} = s\rho u^{\mu} + \frac{q^{\mu}}{T}, \tag{A1}$$

where q^{μ} is the heat flux, s is the entropy per unit mass and T is the temperature of the fluid. The heat flux is given by the relativistic form of Fourier law, namely (Israel 1976)

$$q_{\mu} = -\lambda T \left(h^{\nu}_{\mu} \nabla_{\nu} \ln T + a_{\mu} \right), \tag{A2}$$

where a^{μ} is the four-acceleration of the fluid, λ is the thermal conductivity and $h_{\mu\nu} = g_{\mu\nu} + u_{\mu}u_{\nu}$ is the projector operator in the space orthogonal to the four-velocity u^{μ}. Under the assumption that the fluid has vanishing shear and vanishing bulk viscosity, the entropy-generation rate that follows from equations (A1) and (A2) is given by

$$T \nabla_{\mu} \mathcal{S}^{\mu} = \frac{q^{\mu} q_{\mu}}{\lambda T}. \tag{A3}$$

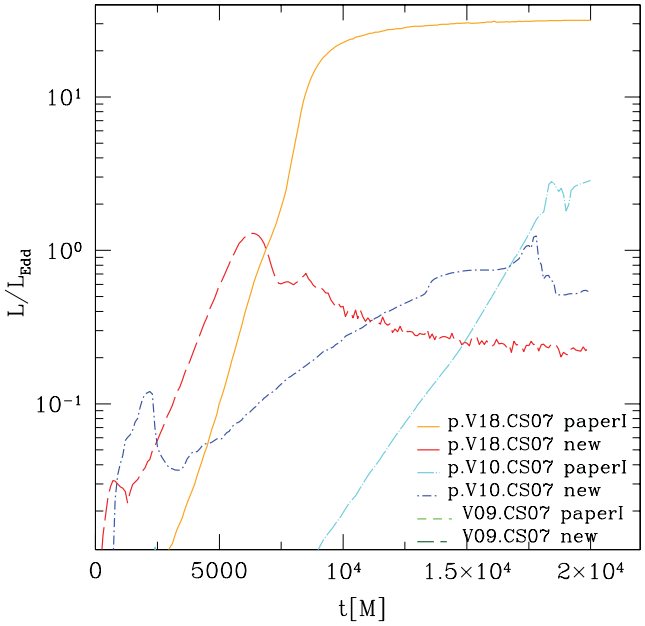

Figure A1. Comparison of luminosity extraction of perturbed BHL – `p.V18.cs07` and `p.V10.cs07`. Extracting the luminosity at $\tau \geq 10$ leads to different light curves; these curves are labelled 'new'. In Paper I we had used the criterion $\tau \geq 1$.

We recall that the thermal conductivity is related to the opacity. For instance, the thermal conductivity computed using the ordinary diffusion approximation of stellar interiors is given by $\lambda = (4/3)a_{\rm rad}cT^3/\chi^{\rm s}$ (Schwartz 1967). Under the assumption that the matter plus radiation fluid behaves as a single fluid with effective pressure and energy density given by $P_{\rm eff} = P + \mathcal{P}_{\rm r}$, $e_{\rm eff} = e + E_{\rm r}$, the four-acceleration a_μ can be computed from the Euler equations as

$$a_\mu = -\frac{h^\nu_\mu \nabla_\nu P_{\rm eff}}{e_{\rm eff} + P_{\rm eff}} \,. \tag{A4}$$

When quasi-stationary configurations are reached, the terms containing time derivatives can be neglected with respect to those containing spatial derivatives, and after replacing q^μ into equation (A3) we obtain

$$\begin{aligned}\nabla_\mu \mathcal{S}^\mu \approx \frac{\lambda}{T^2}\Bigg[&(g^{rr} + \Gamma^2(v^r)^2)(\partial_r T)^2 + (g^{\phi\phi} + \Gamma^2(v^\phi)^2)(\partial_\phi T)^2 + 2\Gamma^2 v^r v^\phi \partial_r T \partial_\phi T - \frac{2T}{e_{\rm eff} + P_{\rm eff}}\Big((g^{rr} + \Gamma^2(v^r)^2)\partial_r P_{\rm eff}\,\partial_r T \\ &+ (g^{\phi\phi} + \Gamma^2(v^\phi)^2)\partial_\phi T\,\partial_\phi P_{\rm eff} + \Gamma^2 v^r v^\phi \partial_r P_{\rm eff}\partial_\phi T + \Gamma^2 v^r v^\phi \partial_\phi P_{\rm eff}\partial_r T\Big) + \left(\frac{T}{e_{\rm eff} + P_{\rm eff}}\right)^2\Big((g^{rr} + \Gamma^2(v^r)^2)(\partial_r P_{\rm eff})^2 \\ &+ (g^{\phi\phi} + \Gamma^2(v^\phi)^2)(\partial_\phi P_{\rm eff})^2 + 2\Gamma^2 v^r v^\phi \partial_r P_{\rm eff}\partial_\phi P_{\rm eff}\Big)\Bigg] \,.\end{aligned} \tag{A5}$$

The conversion of $\nabla_\mu \mathcal{S}^\mu$ from geometrized units to cgs units is given by

$$[\nabla_\mu \mathcal{S}^\mu]_{\rm cgs} = 1.0353 \times 10^{31}\, G\, c \left(\frac{\mathrm{M}_\odot}{M}\right)^3 \left[\nabla_\mu \mathcal{S}^\mu\right]_{\rm geo} \,. \tag{A6}$$

In the code, we generally compute the luminosity as the surface integral over outgoing radiation fluxes $f^r_{\rm r}$ as

$$L = 2\sum_{n=1}^{N_\phi} \left[\sqrt{\gamma}\,\left(f^r_{\rm r}\right)_n\,\Delta\phi_n\right]|_{\tau=\tau_\bullet}, \tag{A7}$$

where $\Delta\phi_n$ is the angular size of a grid cell and the integral is taken at the radial position of the last optically thick surface,[15] i.e. where $\tau = \tau_\bullet$. In Paper I, we computed the luminosity by imposing the criterion $\tau_\bullet \geq 1$. However, these small values of the optical depth often correspond to an integration surface close to the boundary of the numerical domain, where spurious boundary effects may alter the results. Hence, in this paper we have adopted a different criterion by choosing $\tau_\bullet \geq 10$, which guarantees that the integration surface is not placed at the outermost grid cells. For clarification we have repeated the luminosity extraction for two models considered in Paper I, `p.V18.cs07` and `p.V10.cs07`, and show the light curves, computed with the two different criteria, in Fig. A1.

[15] The factor 2 in equation (A7) accounts for both the contributions above and below the equatorial plane.

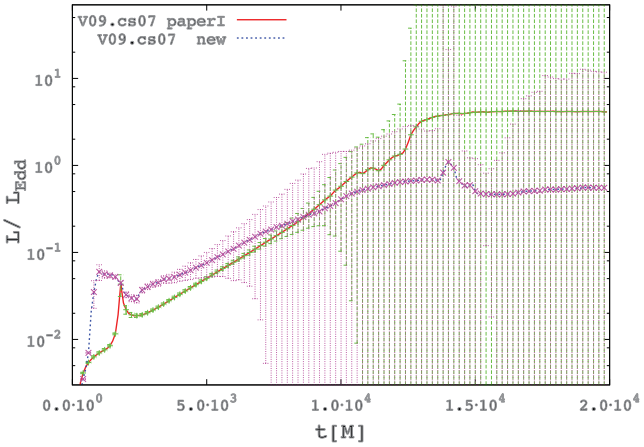

Figure A2. Uncertainties and comparison of luminosity extraction – `V09.cs07`. Extracting the luminosity at $\tau \geq 10$ leads to different light curves with much smaller uncertainties; these curves are labelled 'new'. In Paper I we had used the criterion $\tau \geq 1$.

We can assign error bars to our extraction method by taking the standard deviation of the mean. For model `p.V09.cs07`, the comparison is shown, including the error bars, in Fig. A2. We stress that the size of such error bars reflects the uncertainty in choosing the position of the last optically thick surface across which the emitted luminosity is computed. It should be noted, moreover, that both our estimates agree within these uncertainties, but the choice $\tau \geq 10$ produces much smaller error bars than $\tau \geq 1$ and should therefore be preferred.

APPENDIX B: IMPLEMENTATION OF THE IMEX SCHEME

A tableau notation is usually adopted to express in a compact form the coefficients of the matrices a_{ij}, $\tilde{a}_{ij}$ and of the corresponding vectors ω_i, $\tilde{\omega}_i$ as

$$\begin{array}{c|c} c & a_{ij} \\ \hline & \omega^{\mathrm{T}}, \end{array} \tag{B1}$$

where the index T denotes transposition.[16]

The explicit tableau of the SSP3(4, 3, 3) is

$$\begin{array}{c|cccc} 0 & 0 & 0 & 0 & 0 \\ 0 & 0 & 0 & 0 & 0 \\ 1 & 0 & 1 & 0 & 0 \\ 1/2 & 0 & 1/4 & 1/4 & 0 \\ \hline & 0 & 1/6 & 1/6 & 2/3 \end{array} \tag{B2}$$

while the corresponding implicit tableau is

$$\begin{array}{c|cccc} q_1 & q_1 & 0 & 0 & 0 \\ 0 & -q_1 & q_1 & 0 & 0 \\ 1 & 0 & 1-q_1 & q_1 & 0 \\ 1/2 & q_2 & q_3 & 1/2-q_1-q_2-q_3 & q_1 \\ \hline & 0 & 1/6 & 1/6 & 2/3 \end{array} \tag{B3}$$

with

$$q_1 \equiv 0.241\,694\,260\,788\,21,\ q_2 \equiv 0.060\,423\,565\,197\,05,$$

$$q_3 \equiv 0.129\,152\,869\,605\,90.$$

[16] Note that the coefficients c_i and $\tilde{c}_i$, which are defined as $c_i = \sum_{j=1}^{i} a_{ij}$ and $\tilde{c}_i = \sum_{j=1}^{i} \tilde{a}_{ij}$, are not used in the practical implementation of the scheme.

The coefficients of the radiation matrix $\mathbf{A}(\boldsymbol{Y})$ of equation (37) are given by

$$A_{11} = -\alpha\Gamma[\chi^{\rm t} + \chi^{\rm s} 4W(1-\Gamma^2)],$$
$$A_{12} = \alpha\Gamma v^x[\chi^{\rm t} + \chi^{\rm s} W(1-4\Gamma^2)],$$
$$A_{13} = \alpha\Gamma v^y[\chi^{\rm t} + \chi^{\rm s} W(1-4\Gamma^2)],$$
$$A_{14} = \alpha\Gamma v^z[\chi^{\rm t} + \chi^{\rm s} W(1-4\Gamma^2)],$$
$$A_{21} = -\alpha\Gamma v_x\left[\chi^{\rm t}(1-4W) + 2\chi^{\rm s}(W-1)\right],$$
$$A_{22} = -\alpha\Gamma v^x v_x\left[\chi^{\rm t}(2W-1) + \chi^{\rm s}(2-W)\right] - \alpha(\chi^{\rm t} + \chi^{\rm s})/\Gamma,$$
$$A_{23} = -\alpha\Gamma v^y v_x\left[\chi^{\rm t}(2W-1) + \chi^{\rm s}(2-W)\right],$$
$$A_{24} = -\alpha\Gamma v^z v_x\left[\chi^{\rm t}(2W-1) + \chi^{\rm s}(2-W)\right],$$
$$A_{31} = -\alpha\Gamma v_y\left[\chi^{\rm t}(1-4W) + 2\chi^{\rm s}(W-1)\right],$$
$$A_{32} = -\alpha\Gamma v^x v_y\left[\chi^{\rm t}(2W-1) + \chi^{\rm s}(2-W)\right],$$
$$A_{33} = -\alpha\Gamma v^y v_y\left[\chi^{\rm t}(2W-1) + \chi^{\rm s}(2-W)\right] - \alpha(\chi^{\rm t} + \chi^{\rm s})/\Gamma,$$
$$A_{34} = -\alpha\Gamma v^z v_y\left[\chi^{\rm t}(2W-1) + \chi^{\rm s}(2-W)\right],$$
$$A_{41} = -\alpha\Gamma v_z\left[\chi^{\rm t}(1-4W) + 2\chi^{\rm s}(W-1)\right],$$
$$A_{42} = -\alpha\Gamma v^x v_z\left[\chi^{\rm t}(2W-1) + \chi^{\rm s}(2-W)\right],$$
$$A_{43} = -\alpha\Gamma v^y v_z\left[\chi^{\rm t}(2W-1) + \chi^{\rm s}(2-W)\right],$$
$$A_{44} = -\alpha\Gamma v^z v_z\left[\chi^{\rm t}(2W-1) + \chi^{\rm s}(2-W)\right] - \alpha(\chi^{\rm t} + \chi^{\rm s})/\Gamma,$$

where, just for convenience, we have specified the spatial coordinates to (x, y, z).

This paper has been typeset from a TEX/LATEX file prepared by the author.